Global and Planetary Change xxx (2012) xxx–xxx

Contents lists available at SciVerse ScienceDirect

Global and Planetary Change

journal homepage: www.elsevier.com/locate/gloplacha

Precession-driven monsoon variability at the Permian–Triassic boundary — Implications for anoxia and the mass extinction

Arne Winguth *, Cornelia Winguth

Department of Earth and Environmental Sciences, University of Texas at Arlington, Arlington, TX 76019-0049, United States

ARTICLE INFO

Article history:
Received 31 May 2011
Accepted 18 June 2012
Available online xxxx

Keywords:
Permian
Triassic
climate
orbital
monsoon
extinction
anoxia
modeling

ABSTRACT

By the end of the Late Permian, most continents had collided to form the supercontinent of Pangea. The associated climatic changes at the Permian–Triassic boundary coincided with the most severe mass extinction in the Phanerozoic. One extinction hypothesis favors a climatic response to an increase in large-scale volcanism resulting in ocean stagnation and widespread anoxia with fatal consequences for marine and land organisms. Recent interpretations of geochemical data suggest that orbitally-driven periodic upwelling of toxic hydrogen-sulfide rich water masses contributed to the extinction of species.

In this paper, we use the Community Climate System Model (CCSM3) in order to explore the effect of eccentricity-modulated changes of the precession on the strength of Pangean megamonsoons and their impact on productivity and oxygen distribution. The climate model simulates high variability in monsoonal precipitation, trade winds and equatorial upwelling in response to precessional extremes, leading to remarkable fluctuations in the export of carbon from the euphotic zone and hence reduction in dissolved oxygen concentrations in subsurface layers. These findings are in general agreement with increased primary productivity, intensified euxinia within the oxygen-minimum zone, and decimation of the radiolarian zooplankton community as inferred from Japanese marine sections.

Strong changes in river run-off linked to precipitation oscillations possibly led to a high variability in the nutrient supply to the Tethys Ocean, thus affecting regional productivity and oxygen distribution. The model results suggest that orbital variability in the sedimentary record and the associated extinction of species are related rather to periodic anoxia in near surface-to-intermediate depth than to widespread anoxic events in the Panthalassic deep-sea.

1. Introduction

The Permian–Triassic Boundary (PTB, ~251.5 Ma) is of great interest for global change studies, because it is associated with extreme climatic conditions due to the existence of the supercontinent Pangea and the superocean Panthalassa, and due to strong environmental changes potentially associated with massive volcanism (Campbell et al., 1992; Sobolev et al., 2011). The PTB is characterized by the largest mass extinction of the Phanerozoic, with about 90% of the marine organisms disappearing from the geological record (Raup and Sepkoski, 1982; Erwin, 1994; Sepkoski, 1995; Alroy et al., 2008). The causes of the extinction are still under debate. One of the commonly discussed hypotheses is that ocean stagnation and widespread anoxic conditions occurred (Wignall and Hallam, 1992, 1993; Knoll et al., 1996; Hallam and Wignall, 1997; Isozaki, 1997; Ward et al., 2001; Wignall and Twitchett, 2002; Wignall and Newton, 2003; Kump et al., 2005; Meyer et al., 2008), leading to the extinction of marine organisms (Berner, 2002). Different conclusions have been drawn from studies of Panthalassic deep-sea sections in the Japanese Mino-Tamba Belt. The presence of widespread deep-sea anoxia has been inferred from the sharp transition from organic-poor cherts to black siliceous shales in the uppermost Permian (Wignall and Twitchett, 1996; Isozaki, 1997), and the presence of euxinia at the beginning of this anoxic period has been concluded from the enrichment of framboidal pyrites (Wignall et al., 2010). Algeo et al. (2010), on the other hand, suggest that anoxia at the end of the Permian was restricted to the oxygen minimum zone (OMZ) and that apparent increases in the concentrations of organic matter and trace metals were linked to a loss of biogenic silica flux.

Oxygen consumption by decay of particulate organic matter needs to exceed the oxygen supply by circulation in order to produce anoxia in the deep sea (Winguth et al., 2002; Kiehl and Shields, 2005; Winguth and Maier-Reimer, 2005; Meyer et al., 2008). Changes in the ocean circulation related to changes in the pole-to-equator gradient (Hotinski et al., 2001), a switch from thermal mode to haline mode (Zhang et al., 2001), an increase in greenhouse gas concentrations associated with massive volcanic eruptions, or a combination

* Corresponding author at: Department of Earth and Environmental Sciences, University of Texas at Arlington, 500 Yates St., Arlington, Texas, 76019, United States. Tel.: +1 817 272 2977; fax: +1 817 272 2628.
E-mail address: awinguth@uta.edu (A. Winguth).

0921-8181/$ – see front matter © 2012 Elsevier B.V. All rights reserved.
doi:10.1016/j.gloplacha.2012.06.006

of these factors (Kidder and Worsley, 2010) could have contributed to anoxia in the deep sea.

Superimposed on the dramatic large-scale changes in the climate system are climatic variations due to changes in the Earth's orbit (Kutzbach and Gallimore, 1989; Parrish, 1993; Gibbs et al., 2002; Winguth et al., 2002; Huybers and Aharonson, 2010). For example, precession-modulated upwelling of sulfidic water masses onto a shallow-marine carbon platform has been inferred from pyrite sedimentation rates and carbonate $\delta^{13}C$ records in the PTB section at Nhi Tao, Vietnam (Algeo et al., 2007). Other possible explanations for the observed geochemical changes include upward excursions of the chemocline, resulting in H_2S poisoning of surface waters (Kump et al., 2005), or deposition of sulfur by volcanism (Strauss, 1997; Algeo et al., 2007).

The relevance of orbital forcing for environmental changes at the PTB is supported by magnetic susceptibility data from Shangsi, southern China (Huang et al., 2011). Orbital pacing of Pangean climate is also inferred from cyclical lacustrine rocks (Newark Section; Olsen and Kent, 1996) in the Triassic subtropics (near 10°). Since the subtropics to mid-latitudes of Pangea are greatly affected by eccentricity-modulated precessional cycles (Crowley et al., 1992), peak eccentricity values may have intensified the monsoonal circulation, as inferred from varve sediments from the Castile Formation in western tropical Pangea (Anderson, 2010). The large continental configuration of Pangea favored strong seasonal variability in the subtropics (Barron and Fawcett, 1995), with extreme precipitation during the summer, referred to as megamonsoons (Kutzbach and Gallimore, 1989). The extreme monsoonal climate for both hemispheres across the Pangean continent has also been inferred from a Late Permian climate comparable to that of the present-day savannah in the Chinle Formation of the Colorado Plateau (Daugherty, 1941), from the global distribution of red beds, evaporites, and coal deposits during the Triassic (Robinson, 1973), and from the fact that landmasses similar to present-day Eurasia were present in both hemispheres (Parrish, 1993; Ziegler et al., 2003).

In this study, we investigate the response of the strength of the monsoonal circulation, and related changes in ocean circulation, productivity and dissolved oxygen distribution to changes in Earth's orbital parameters for the end-Permian. In particular, we examine the influence of extremes in the precessional cycle on nutrient availability and productivity in the euphotic zone either directly through fluctuations in the ocean circulation or indirectly through intensification in the seasonal precipitation leading to enhanced weathering.

2. Climate model and experiments

2.1. The Community Climate System Model (CCSM3)

The end-Permian climate simulations have been carried out with the NCAR CCSM3, a global coupled climate model including the ocean, atmosphere, sea ice, and land surface (Kiehl and Shields, 2005; Collins et al., 2006a; Yeager et al., 2006; and references therein). A spectral horizontal resolution of T31, corresponding to an equivalent grid spacing of approximately 3.75°×3.75° in latitude and longitude, and vertically 26 unevenly spaced terrain-following levels (Collins et al., 2006b), has been chosen for the atmosphere to allow long-term integrations. Correspondingly, the ocean is resolved by a nominal 3° horizontal grid and by 25 layers in the vertical direction (Gent et al., 2006).

The marine carbon component of the coupled climate-carbon cycle model is based upon the Ocean Carbon Model Intercomparison Project (OCMIP) (Doney et al., 2006; Najjar and Orr, unpublished manuscript; http://www.ipsl.jussieu.fr/OCMIP/) and is described in Winguth and Winguth (2012) for the Permian application. The model estimates air–sea fluxes of CO_2 with the wind-dependent gas exchange coefficient (Wanninkhof, 1992) across the air–sea interface, the temperature-dependent solubility of CO_2, and the difference between the prescribed pCO_2 of the atmosphere and the pCO_2 of the uppermost layer of the ocean (Doney et al., 2006). The ocean carbon cycle model predicts seven prognostic variables, i.e. phosphate (PO_4), total dissolved inorganic iron, dissolved organic phosphorus and iron, dissolved inorganic carbon, total alkalinity, and dissolved oxygen, that are transported by the ocean model. The parameterization of biological uptake of nutrients is similar to that used in the Hamburg Model of the Ocean Carbon Cycle (HAMOCC; Maier-Reimer, 1993) and assumes a constant Redfield ratio for particulate organic matter. The uptake of PO_4 is given by the turnover of biomass, modulated by surface solar irradiance, temperature, and macro- and micronutrients. The carbon cycle model uses a single Martin power-law curve to describe the vertical particulate organic phosphorus flux profile over the full water column.

2.2. Late Permian boundary conditions

To the basic Permian geography from Kiehl and Shields (2005), a mid-ocean ridge has been added in this study (Osen et al., 2012). The shape of the mid-ocean ridge is similar to that of the modern East Pacific Rise with a fast spreading rate of ~10 cm/yr; its profile and height have been computed after Stein and Stein (1992). The ridge bends at approximately 80°N towards what is present-day Siberia, near the area of the Siberian Trap eruptions. The mid-ocean ridge simulation enhanced vertical mixing and topographic steering of the currents near the ridge-axis, but changes in the global distribution of water masses and circulation in the Panthalassa are insignificant when compared with the simulation using a flat bottom (see Osen et al., 2012).

The solar constant applied for the latest Permian is 1338 W m^{-2}, ~2.1% lower than the modern value. Following the study of Kiehl and Shields (2005), greenhouse gas concentrations were set to 0.7 ppmv for pCH_4, 0.275 for pN_2O, and 3550 ppmv for atmospheric pCO_2 (based on Kidder and Worsley, 2004), ~12.7× higher than the preindustrial level (PAL) of 280 ppmv, corresponding to a radiative forcing of 16 W m^{-2}. The reconstructions of greenhouse gas concentrations or the end-Permian remain uncertain because of the unknown amount of carbon injection due to Siberian Trap volcanism-induced metamorphism of organic matter and petroleum (Svensen et al., 2009). The maximum end-Permian greenhouse gas concentration of ~12–13× PAL, as inferred from soil carbonate CO_2 paleobarometers (Cerling, 1991), and consistent with estimates by Kidder and Worsley (2004), have recently been revised by Breecker et al. (2010) who propose a lower end-Permian value of ~4–5× PAL, in agreement with the GEOCARBSULF model. Such low estimates, however, are inconsistent with emission estimates from the Siberian Traps, successive Late Permian and Early Triassic spikes of unusually high atmospheric CO_2 inferred from stomatal indices, lycopsid spore diversity, and leafy stem diameters (Retallack et al., 2011) and also in disagreement with the frost-free polar climates inferred from sensitive sedimentary deposits (Ziegler et al., 1998). The prescribed land vegetation types are taken from Kiehl and Shields (2005) and based on surface types from Rees et al. (1999). Present-day conditions are applied for all other boundary conditions and parameterizations.

2.3. Description of the climate simulations

The orbital settings used in this study (Table 1) follow the concept of Sloan and Huber (2001) and are consistent with recent estimates by Laskar et al. (2004). The two scenarios capture extreme orbital settings, referred to as P− with the precessional cycle at its minimum value, and P+ with the precessional cycle at its maximum value. The first scenario (P−) is characterized by a reduced, the second scenario (P+) by an enhanced seasonal cycle. For the P− scenario, the precession of the equinox is set to 90° (prograde angle between the perihelion and the vernal equinox), the eccentricity modulating the

Please cite this article as: Winguth, A., Winguth, C., Precession-driven monsoon variability at the Permian–Triassic Implications for anoxia and the mass extinction, Glob. Planet. Change (2012), doi:10.1016/j.gloplacha.2012.06.006

Table 1
Orbital parameter choices for the experiments.

Experiment	Orbital parameters		
	Eccentricity	Precessional angle	Obliquity
P−	0.0531	90	22.8
P+	0.0524	270	23.8

precession to 0.0531, and the obliquity to 22.8°. The P+ scenario corresponds to an additional shift of the precession of the equinox by 180° (or ~11,500 yr later) to 270°, with eccentricity set to 0.0524 and obliquity set to 23.8°. With these conditions, the Earth's orbit is in a perihelion, nearest to the Sun, during summer solstice and in an aphelion, farthest from the Sun, during winter solstice. The eccentricity and obliquity are altered in the P+ scenario because of the progress in time with the shift of the precession of the equinox. As shown in Fig. 1, the largest differences in incoming solar radiation occur in the polar regions.

All model simulations are integrated over 3000 yr (Fig. 2) with initial conditions taken from a 5000 yr control integration, using the physical settings of Kiehl and Shields (2005). The output from the modeling simulations discussed in the sections below represents 100-yr averages for the two seasons: June, July, and August (JJA) and December, January, and February (DJF).

3. Orbitally-induced changes in seasonality and monsoon intensity

3.1. Response of the atmosphere to orbital changes

Seasonal climatic variations of Pangea show a remarkable continentality, with temperatures in Gondwana ranging from −25 °C in the polar regions during the winter months to >45 °C in the subtropics during the summer months (Fig. 3 A and B). This temperature range is in agreement with previous studies using either an idealized continental configuration (Kutzbach and Gallimore, 1989) or a realistic geographic configuration (Gibbs et al., 2002; Winguth et al., 2002). In contrast to the previous studies, overall temperatures are higher by ~5–10 °C because of the higher atmospheric CO_2 concentration (12.7× PAL) and hence stronger CO_2 radiative forcing (16 W m^{-2}). During the southern winter (Fig. 3A), the continental climate of Gondwana leads to sea ice formation limited to nearshore areas of the Pangean east coast, with a sea ice fraction of <60%. Dropstones and rhythmites as indicators of such a cold climate have been identified in the geological record of Tasmania along the southeastern coast of Gondwana for the Wordian, but not for the Tutorian (Ziegler et al., 1998).

Precessional variations cause out-of-phase changes between the hemispheres for the winter and summer seasons and are exactly reversed from that of the tilt. The difference in surface air temperature between the scenarios with maximal (P+) and minimal (P−) precessional setting for the two seasons is shown in Fig. 3. For JJA, the Earth is in the perihelion and air temperature anomalies of up to +10 °C are centered over Laurasia at ~45°N and of +8 °C over Gondwana at ~15°S (Fig. 3C), whereas for the aphelion (DJF), the temperature anomalies with maximal values of about −8 °C are centered over Pangea at 15°N and 45°S (Fig. 3D). Surface temperature response to variations in precession is a function of the land–sea distribution (Crowley and North, 1991; Sloan and Huber, 2001), with lower variation over the ocean due to the higher heat capacity of the water. This explains why changes in the polar regions are relatively small, although precession-induced insolation fluctuations are maximal. In June, the latitude of 45°N receives ~100 W m^{-2} more radiation under the P+ scenario than under the P− scenario (Fig. 1), leading to a significant warming over Laurasia (Fig. 3C). In January, the subtropics to mid-latitudes gain ~75 W m^{-2} more radiation in the P− scenario so that Gondwana becomes warmer (Fig. 3D).

The distribution of sea level pressure and wind for the winter and summer season is affected by the seasonal variations in insolation and regional fluctuations associated with the monsoon (Fig. 4). In the P− scenario, the intertropical convergence zone (ITCZ) is shifted to ~10°N in the boreal summer and to ~10°S in the boreal winter. Strong trade winds result from a high-pressure system over the Panthalassa at 35° during the summer in the P− simulation (Fig. 4A). With the more extreme precessional setting (P+), NE trade winds are reduced in the northwestern Panthalassa due to the weakening of the high pressure system (Fig. 4C) in response to the orbitally-induced decrease in the meridional surface temperature gradient (Figs. 1 and 3C) and thus a reduced meridional temperature gradient from the tropics to the mid-latitudes, whereas in the austral summer trade winds are intensified accordingly.

Superimposed over the Hadley circulation is a pronounced summer monsoon circulation transporting moist air from the western Tethys Ocean to a low pressure ridge over the Pangean subtropics with 990 hPa centered at ~25°N in JJA and 980 hPa centered at 35°S in DJF in the P− scenario (Fig. 4B). The winter monsoon high (1020 hPa) in the northern hemisphere in this simulation is located at 35°N with near-gale northeasterly winds, and in the southern hemisphere, south-easterlies are directed towards the western Tethys Ocean. The difference in strength of the wind between the summer and winter monsoon can be related to the strong north–south temperature contrast during the winter months (Figs. 3A and B), while during the summer months, these gradients are substantially weaker (Kutzbach and Gallimore, 1989).

In the P+ scenario in summer, the Pangean subtropical low pressure system in the northern hemisphere is reduced by 5–10 hPa relative to the P− scenario (Fig. 4C) in response to the increase in the surface temperature (Fig. 3C), whereas in the southern hemisphere the low pressure rises to 990 hPa (Fig. 4D) in reaction to the decline in temperature (Fig. 3D).

The precipitation patterns (Fig. 5) are non-linearly correlated to the changes in temperature and pressure. Updraft of moist tropical air masses along the ITCZ causes strong precipitation of over 8 mm/day during the summer months. In the P− experiment, tropical precipitation is particularly high in western Panthalassa and in the Tethys Ocean with highest sea surface temperatures.

For both orbital scenarios, monsoonal precipitation experiences a high seasonal variability with high precipitation over northern tropical Pangea and extreme rainfall over North China during the summer months

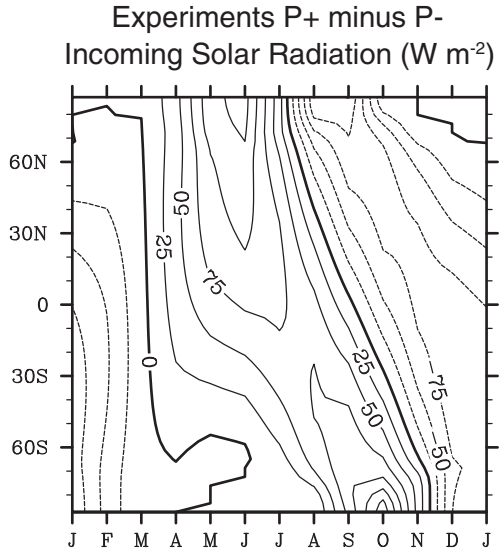

Fig. 1. Differences of monthly incoming solar radiation at the top of the atmosphere for experiments P+ minus P−. Contour interval is 25 W m^{-2}; dashed lines are negative values.

Please cite this article as: Winguth, A., Winguth, C., Precession-driven monsoon variability at the Permian–Triassic Implications for anoxia and the mass extinction, Glob. Planet. Change (2012), doi:10.1016/j.gloplacha.2012.06.006

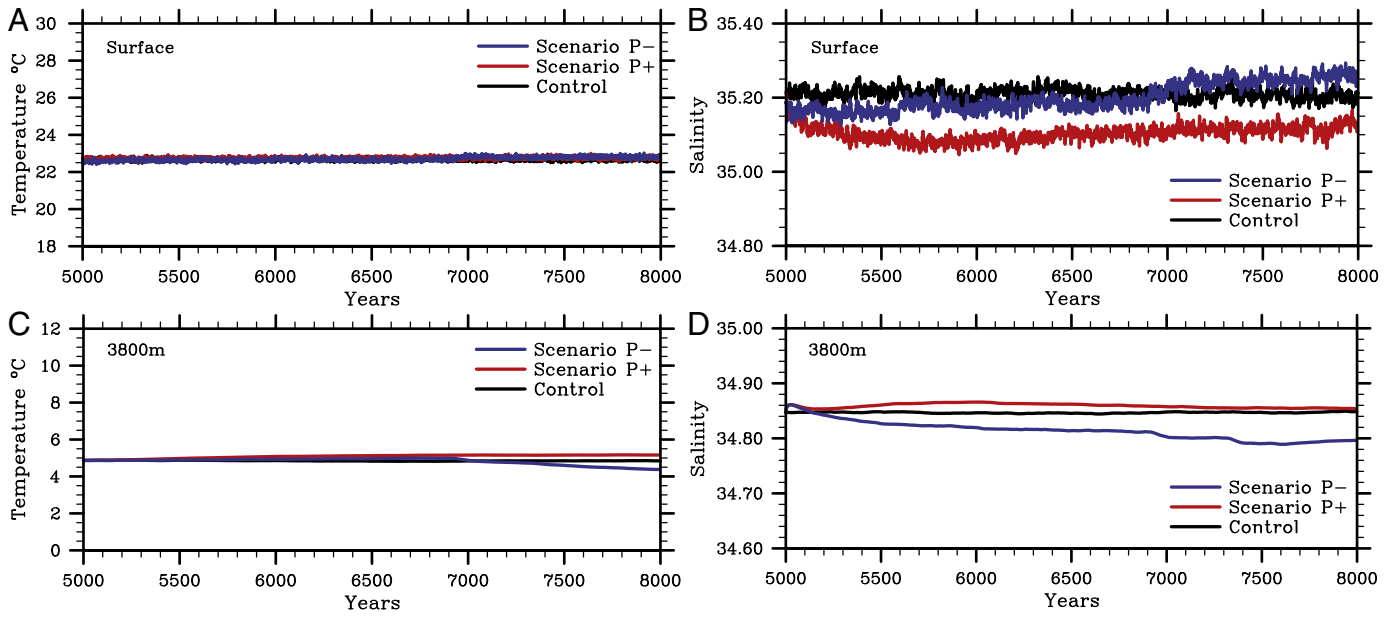

Fig. 2. Time series of the global mean sea surface temperature (in °C) (A), and salinity (B), and of the global mean deep-sea temperature (C) and salinity (D) for the scenario with maximal precession (P+) (red) and with minimal precession (P−) (blue). The control scenario (black) uses orbital settings from Kiehl and Shields (2005). Time series have been smoothed with a 5-yr running mean.

(>10 mm/day) and dry conditions during winter (<1 mm/day). The high orbitally-induced variability in precipitation over the subtropical Pangean continent is also supported by fluctuations in levels of the expanding playa lake system in the southern Permian Basin (Bailey, 2001). During the austral summer, rain patterns shifted to the southern tropical–subtropical region, particularly over the Tethys Ocean including South China and the east coast of Gondwana. These findings are in agreement with Late Permian climate-sensitive sediments (Ziegler et al., 1997), for example coal deposits in China (Zhou and Ren, 1981) and on islands in the southern Tethys (Ziegler et al., 2003).

The shift to a more extreme eccentricity (P+ scenario) produces an increase in the monsoonal precipitation across subtropical Pangea, thus creating a negative feedback on the surface temperature. These changes can be explained by the higher surface radiative forcing in P+ during JJA, which leads to enhanced evaporation, an increase in cloud cover, and precipitation over northeastern tropical Pangea,

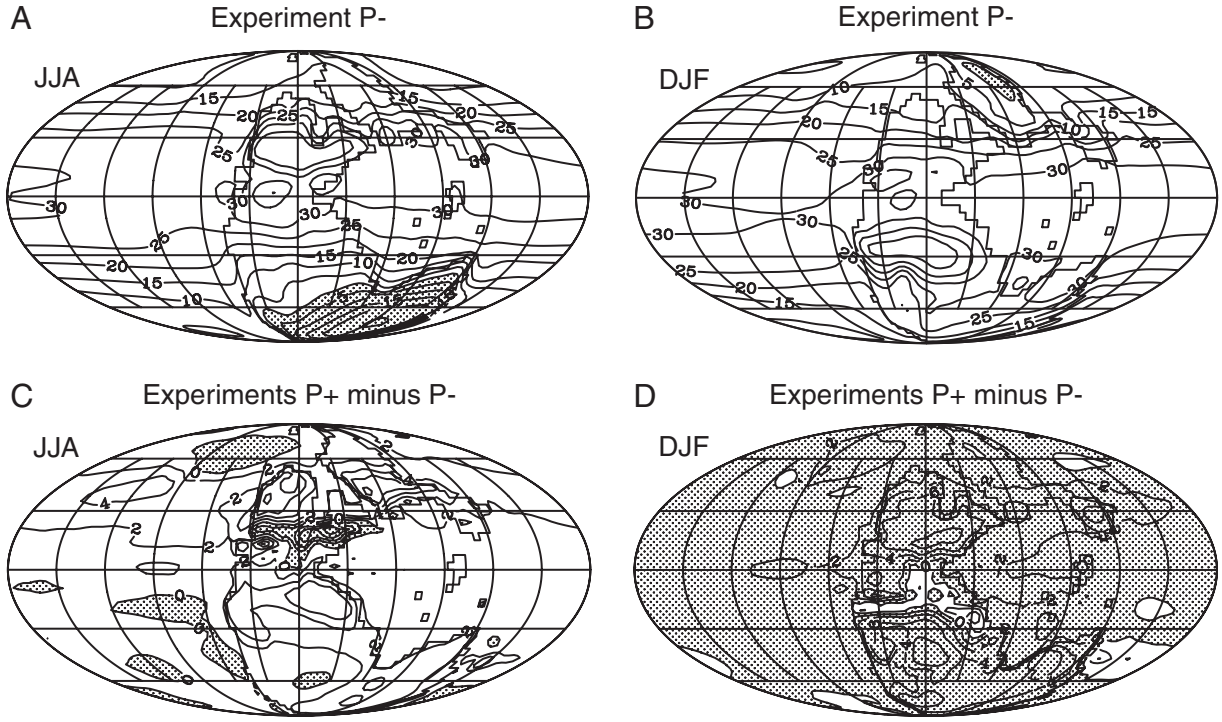

Fig. 3. Surface air temperatures (in degree Celsius) for two seasons for the scenario with minimal precessional setting (P−): (A) DJF and (B) JJA (contours are shown in 5 °C intervals) and difference in surface air temperatures for DJF (C) and JJA (D) between the scenarios with maximal (P+) and minimal (P−) precessional setting (contours are shown in 2 °C intervals).

Please cite this article as: Winguth, A., Winguth, C., Precession-driven monsoon variability at the Permian–Triassic Implications for anoxia and the mass extinction, Glob. Planet. Change (2012), doi:10.1016/j.gloplacha.2012.06.006

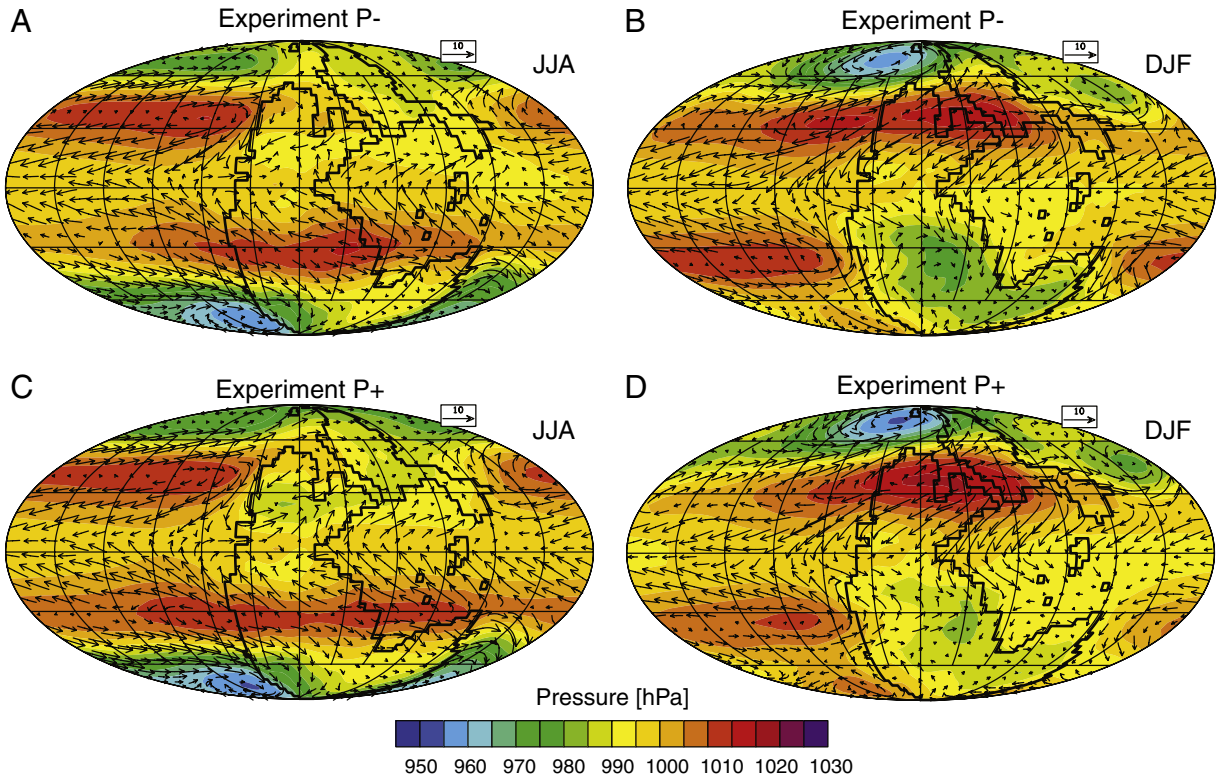

Fig. 4. Sea level pressure (in hPa) and surface wind speeds (in m s^{-1}) for two seasons for the scenarios with maximal (P+) and minimal (P−) precessional setting: (A) JJA for case P−, (B) DJF for case P−, (C) JJA for case P+, and (D) DJF for case P+. Contours are shown in 5 hPa intervals. Reference vector in upper right corner of graphs represents 10 m s^{-1}.

resulting in surface cooling (Fig. 3A). Incoming radiation is reduced at the surface by the higher amount of reflected and absorbed incoming radiation by clouds, and heat loss from the surface is increased by evaporation. Correspondingly, tropical anomalies in DJF are damped as shown in Fig. 3B and Fig. 5B.

3.2. Response of the ocean to orbital changes

The sea surface temperature and the surface velocity (Fig. 6) show a significant response to orbital variations in solar radiation, particularly in mid-latitudes (around 45°) in the central North Panthalassa, with

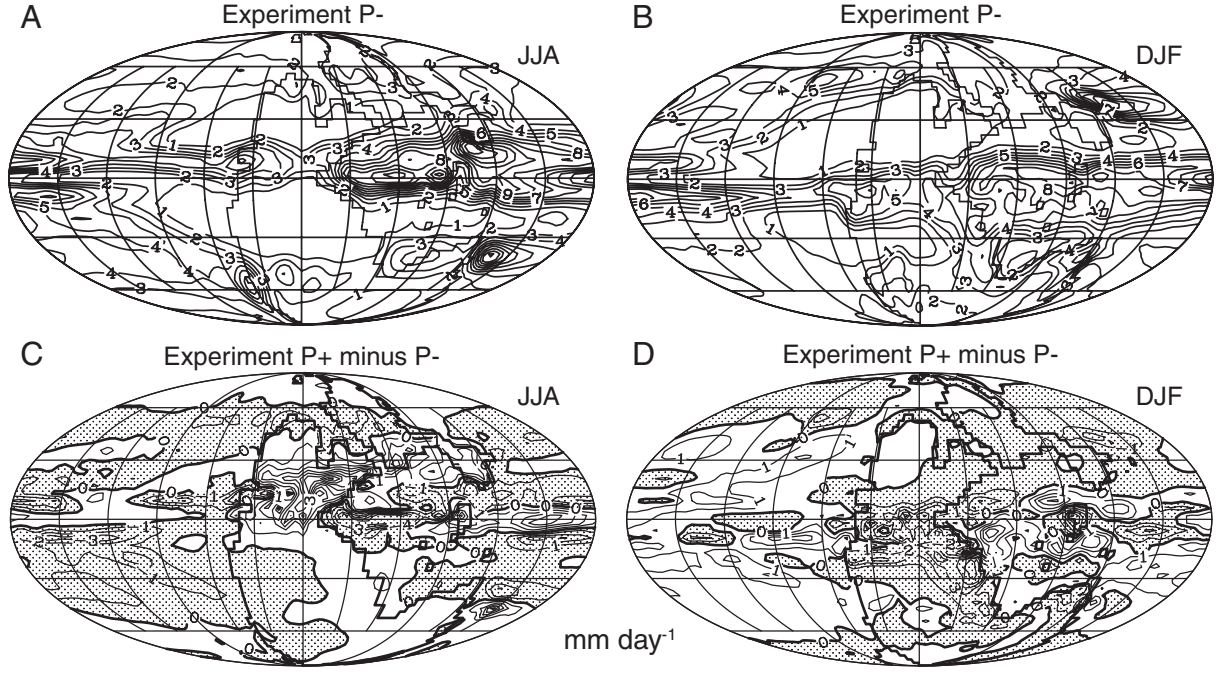

Fig. 5. Precipitation (in mm day^{-1}) for two seasons for the scenarios with maximal (P+) and minimal (P−) precessional setting: (A) JJA for case P−, (B) DJF for case P−, (C) JJA for case P+, and (D) DJF for case P+. Contours are shown in 5 hPa intervals.

Please cite this article as: Winguth, A., Winguth, C., Precession-driven monsoon variability at the Permian–Triassic Implications for anoxia and the mass extinction, Glob. Planet. Change (2012), doi:10.1016/j.gloplacha.2012.06.006

temperatures during the summer months being ~4 °C warmer in the P+ experiment relative to the P− experiment. These fluctuations are linked to a 75 W m^{-2} higher insolation at the top of the atmosphere, and lower cloud cover in the center of the high pressure system. In the southern hemisphere, a positive temperature anomaly for JJA appears off the east coast of Gondwana (Fig. 6A), likely related to wind stress changes associated with the intensification of the high-pressure ridge, increased heat flux to the atmosphere, and thus increased precipitation.

With mid-latitude sea surface temperatures being warmer in the P+ scenario than in the P− scenario (Fig. 6A) for JJA, NE trade winds are less intense, and thus Ekman-induced upwelling is reduced (Fig. 7A). The reduced upwelling and increased solar forcing in the P+ scenario produce a pronounced increase in eastern tropical sea surface temperatures of >2 °C (Fig. 6A).

The situation in the boreal winter (DJF) is approximately the reverse of the boreal summer for the P+ scenario. A decrease in incoming shortwave radiation (Fig. 1) leads to global cooling (Fig. 6B). Orbitally-driven changes yield a more pronounced high-pressure system over central northern Pangea in the P+ scenario. In response to the intensification of the winter high pressure over land, the NE trades passing the equator are stronger (Fig. 4D), leading to an increase in upwelling (Fig. 7B) and thus surface cooling in the eastern Panthalassa (Fig. 6B). Over the southern polar Panthalassa, positive temperature anomalies are related to an increased advection of warmer water masses from the mid-latitudes.

The lower global surface salinity in the P+ scenario (Fig. 2 B) compared to the P− scenario is linked to a higher precipitation in the tropics and high latitudes, but slightly warmer subtropics in the P+ scenario (Fig. 6) yield an increase in evaporative flux to the atmosphere. The intensification of subtropical surface salinity, strengthening the deep water sources in the subtropics, and the increased stratification due to enhanced fresh water fluxes from the atmosphere, produce a small increase in deep-sea temperature (0.8 °C) and salinity (0.06) (Fig. 2C and D).

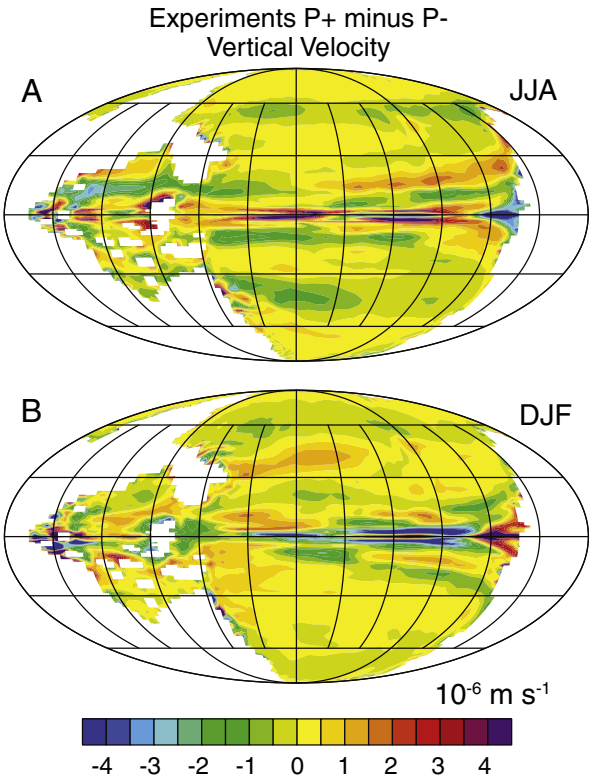

Fig. 7. Difference in vertical velocity at ~100 m depth (in 10^{-6} m s^{-1}) for the two seasons between the scenarios with maximal (P+) and minimal (P−) precessional setting: (A) JJA and (B) DJF. Positive values denote changes in upward direction (increased upwelling or decreased downwelling). Upwelling is increased in JJA in the eastern equatorial Pacific whereas in DJF, upwelling is decreased. Contours are shown in 0.5 m s^{-1} intervals.

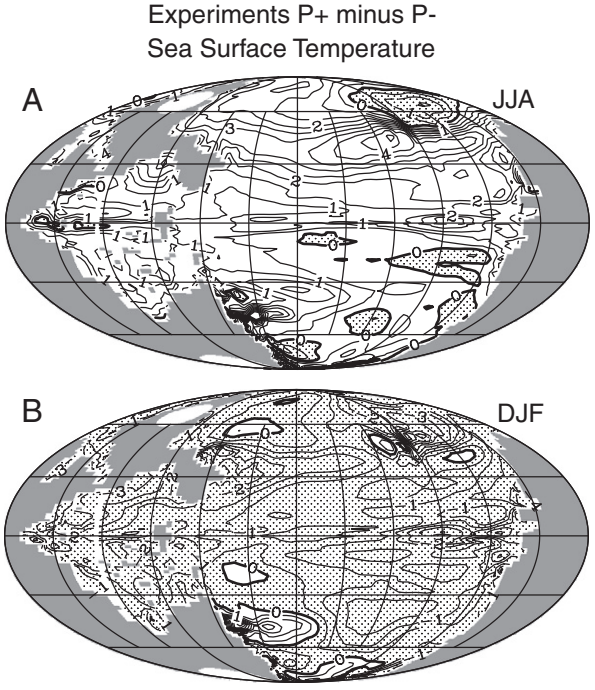

Fig. 6. Difference in sea surface temperatures (in degree Celsius) for two seasons between the scenarios with maximal (P+) and minimal (P−) precessional setting: (A) JJA and (B) DJF. Contours are shown in 0.5 °C intervals.

3.3. Orbital-scale control of the poleward heat transport

The zonal average profile of net radiation for annual mean conditions at the top of the atmosphere (Q_{TA}) can be estimated by the total poleward heat transport in the ocean–atmosphere system (T_{AO}) as a sum of the poleward heat transport by the atmosphere (T_A) and by the ocean (T_{OC}). As reviewed by Collins et al. (2006a), it is very difficult to achieve a precise time-average energy balance for Q_{TA} and thus small losses and gains are predicted. For CCSM3 under present-day boundary conditions, the annual mean rms of Q_{TA} is −0.21 W m^{-2} (Collins et al., 2006a), and for the scenarios P+, P−, and control the rms reduces to −0.05 W m^{-2} because of the long-term integration. These values are in the range of the observational uncertainty of about 0.8 W m^{-2} (Oort and Peixoto, 1983). Global annual mean and zonally averaged heat transport for the P+ scenario, P− scenario and control run are compared to the present-day derived estimates from the National Center for Environmental Prediction (NCEP) (Fig. 8). The atmospheric poleward heat transport poleward of 30° dominates the total heat, whereas the oceanic heat transport is strongest at 10–20° in the southern hemisphere, contrary to the present-day scenario (Fig. 8D). The difference between the PTB (Fig. 8A–C) and the present-day poleward ocean heat transport (Fig. 8D) is related to the fact that for the present-day, ocean heat transport in the South Atlantic is directed northward and the large land masses are located in the northern hemisphere, contrary to the Permian. The positive temperature difference in the northern hemisphere mid-latitudes can be attributed to a stronger poleward ocean heat transport in the P+ scenario, whereas the positive temperature difference in the southern hemisphere mid-latitudes is related to a stronger poleward ocean heat transport in the P− scenario (Fig. 6).

Please cite this article as: Winguth, A., Winguth, C., Precession-driven monsoon variability at the Permian–Triassic Implications for anoxia and the mass extinction, Glob. Planet. Change (2012), doi:10.1016/j.gloplacha.2012.06.006

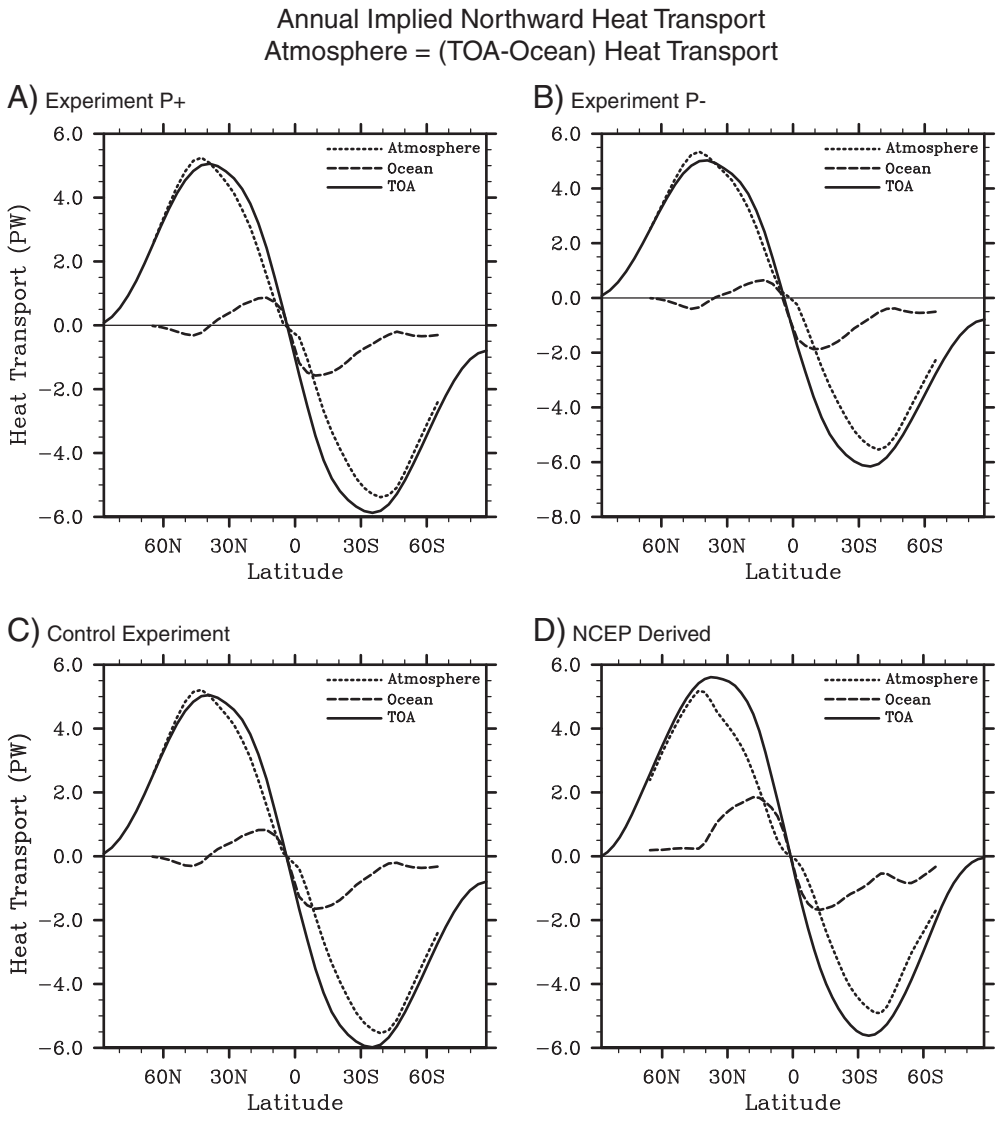

Fig. 8. Meridional profile of the poleward heat transport in PW (10^{15} W). Heat transport by the ocean (T_{OC}), atmosphere (T_A) and total heat transport ($T_{AO} = T_A + T_{OC}$) for the PTB climate for the (A) P+ scenario, (B) P− scenario, (C) control scenario, and (D) the NCEP-derived present-day estimate for comparison.

4. Orbitally-induced changes in marine productivity

The simulated pattern of marine productivity (Fig. 9) is linked to the distribution of temperature (Fig. 6), light, nutrient availability and mixing (Berger, 1978) and thus predominantly controlled by the seasonal cycle. Nutrient supply and mixing are generally the most important factors in regions with sufficient light availability. The marine productivity increases by ~1% with a temperature rise of 1°C (for a 20 °C water mass). In the eastern equatorial Panthalassa, export production (Fig. 9) is pronounced associated with Ekman-induced upwelling of nutrient-rich waters from the subsurface. Seasonally strong productivity during the winter months is simulated for mid-latitudes along the east coast of Pangea at ~45° in response to enhanced wind-driven mixing and a deepening of the mixed layer, comparable with present-day high-productivity zones during the winter in the western Pacific near the Asian continent.

The orbitally-induced changes of productivity in the eastern equatorial Panthalassa are linked to variations in temperature and upwelling. With sea surface temperatures being warmer in the P+ scenario than in the P− scenario for summer (JJA; Fig. 6A), upwelling is reduced (Section 3.2.), leading to a decline in nutrient availability and productivity (by >3 mol C m^{-2} yr^{-1}). For the boreal winter (DJF), an increase of wind-driven equatorial upwelling intensifies the transport of nutrients from subsurface waters to the surface and thus enhances productivity.

With extreme precessional settings, export production is significantly increased at ~45° near the eastern cost of Gondwana and Northern China. Near Gondwana, the mixed layer depth increases in the austral winter (JJA) from ~170 m to ~350 m, leading to a stronger nutrient supply to the euphotic zone and thus enhanced marine production (Fig. 9C). The increase in productivity at ~45°N during the boreal winter (DJF) is also related to changes in coastal upwelling and the intensification and southward shift of the subpolar low pressure system in the P+ case (Figs. 4D and 9D).

5. Seasonal and orbitally-induced variability of oxygen distribution

The simulated vertical oxygen distribution and its variability approximately at the equator are shown in Fig. 10. The vertical organic carbon flux in response to the high equatorial export production of 12 ± 2 mol C m^{-2} yr^{-1} produces the lowest oxygen concentration in the intermediate water masses in the Panthalassa. Most of the tropical ocean is well oxygenated at intermediate depths, with values of 160 μmol L^{-1} in the Tethys and western region of the Panthalassa,

Please cite this article as: Winguth, A., Winguth, C., Precession-driven monsoon variability at the Permian–Triassic Implications for anoxia and the mass extinction, Glob. Planet. Change (2012), doi:10.1016/j.gloplacha.2012.06.006

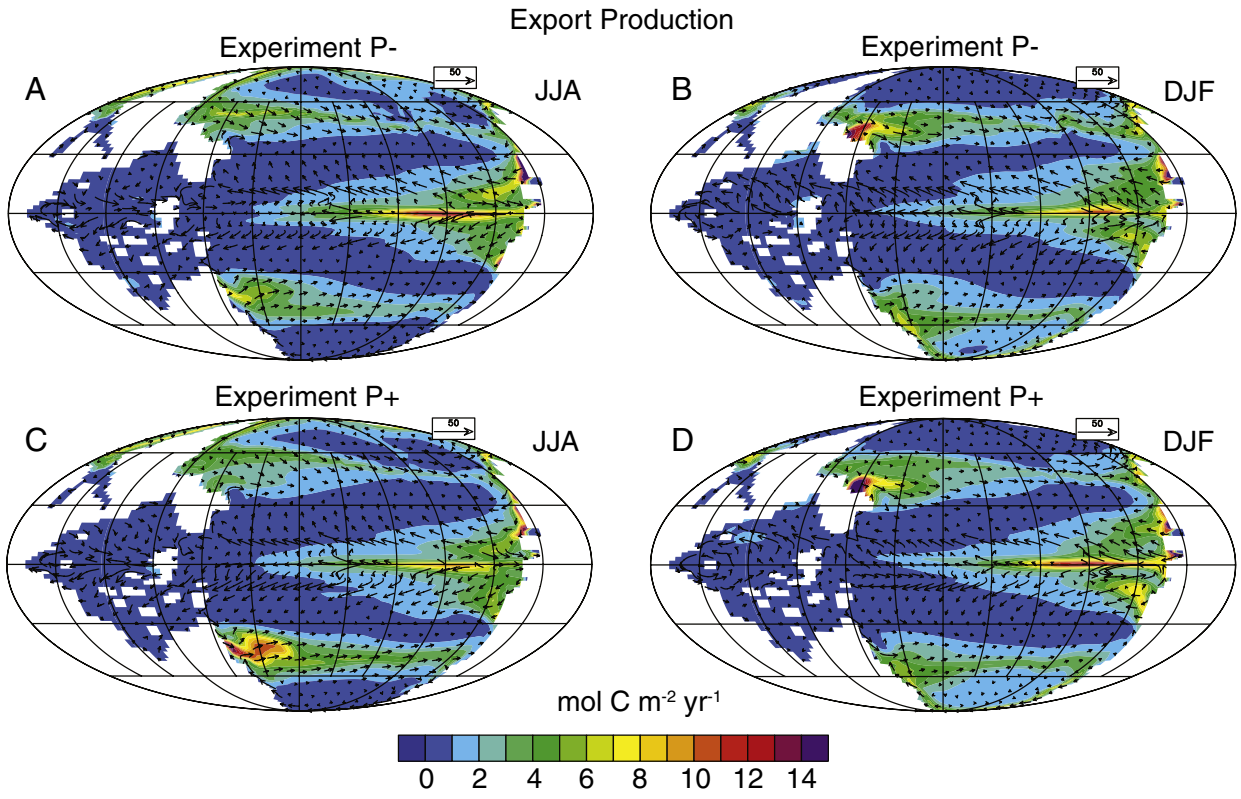

Fig. 9. Export production (in mol C m^{-2} yr^{-1}) and surface current speeds (in cm s^{-1}) for two seasons for the scenarios with maximal (P+) and minimal (P−) precessional setting: (A) JJA for case P−, (B) DJF for case P−, (C) JJA for case P+, and (D) DJF for case P+. Contours are shown in 1 mol C m^{-2} yr^{-1} intervals. Reference vector in upper right corner of graphs represents 50 cm s^{-1}.

becoming less oxygenated towards the high productivity zones in the eastern region of the Panthalassa (Fig. 10A) with lowest values of <5 μmol L^{-1} in the OMZ between 400 and 800 m. The simulated oxygen gradients at intermediate depths are comparable to the high-gradient case of Hotinski et al. (2001), the well-mixed circulation for the thermal mode of Zhang et al. (2001), and the modeling study of Winguth et al. (2002), although the global meridional overturning circulation (MOC) of ~10 Sv (1 Sv = 10^6 m^3 s^{-1}) for the deep sea in this study is significantly more sluggish than the southern hemispheric circulation cell of >80 Sv simulated by Hotinski et al. (2001). A possible explanation for this paradox is that the interaction of export production and equatorial upwelling (Najjar et al., 1992) has a stronger impact on the OMZ for the Late Permian than the strength of the deep-sea circulation. With a total breakdown of the MOC, the deep sea might have become anoxic, as shown in the study of Zhang et al. (2001). However, in this study the deep-sea remains well ventilated, resulting generally in high oxygen concentrations.

The model simulates a pronounced seasonal variability in the dissolved oxygen concentration for the eastern equatorial Panthalassa (up to 10 μmol L^{-1} in 200 m depth; Fig. 10B), related to variations in wind-driven upwelling and productivity, and comparable to the present-day range (World Ocean Atlas; Garcia et al., 2010).

Consistent with the seasonal changes, the largest orbitally-induced fluctuations of oxygen are simulated for the eastern equatorial Panthalassa. In the boreal summer (JJA), the P+ case oxygen concentration is increased by up to 20% in the OMZ compared to the P− case because of a decrease in productivity and vertical particle flux of organic matter (Section 4), whereas for DJF it is decreased by the same amount, but changes are limited to the upper 200 m. The influence of orbital cycles below the OMZ is negligible.

In the Tethys Ocean, the strongest orbital-scale variation of oxygen concentration, reaching up to 20%, is modeled near South China. These fluctuations are linked to wind-induced changes in upwelling and hence productivity along the west coast of the island.

6. Discussion

The model simulations in this study support the hypothesis that Milankovitch cycles have a remarkable impact on the Pangean climate and its variability. The land temperature during the summer months becomes warmer and the thermal cross-equatorial contrast between the Tethys and Laurasia is enhanced during the precessional extreme in solar radiation. The increase in temperature gradient causes an increase in moisture transport to the Pangean continent and thus an enhanced monsoonal circulation. This simulated monsoon intensification is in agreement with idealized concepts of the Pangean monsoonal circulation (Parrish, 1993) and with the orbital pacing that has been inferred from Triassic lake sediments in the Newark Section (Olsen and Kent, 1996).

The changes in precessional forcing do not only affect the precipitation patterns in the Tethys region, but also over western tropical Pangea. The simulated amplifications of the summer monsoon under extreme precessional settings are consistent with the variability of lacustrine sediments from the Castile Formation (Anderson, 2010). Rising temperatures over Pangea lead to advection of warm moist air masses from the eastern Panthalassa, resulting in enhanced precipitation and with that probably increased weathering and eutrophication of the adjacent Tethys Ocean. Orbitally modulated enhancement of weathering might have generated oceanic nutrient pulses (Algeo and Twitchett, 2010), an ecosystem shift (Broecker and Peacock, 1999), and a decline in the abundance of marine eukaryotic algae at the PTB (Knoll et al., 2007).

Modeling studies have demonstrated that a drastic increase in nutrient supply to the ocean could have led to oxygen depletion (Winguth and Winguth, 2012) or even euxinia (Meyer et al., 2008)

Please cite this article as: Winguth, A., Winguth, C., Precession-driven monsoon variability at the Permian–Triassic Implications for anoxia and the mass extinction, Glob. Planet. Change (2012), doi:10.1016/j.gloplacha.2012.06.006

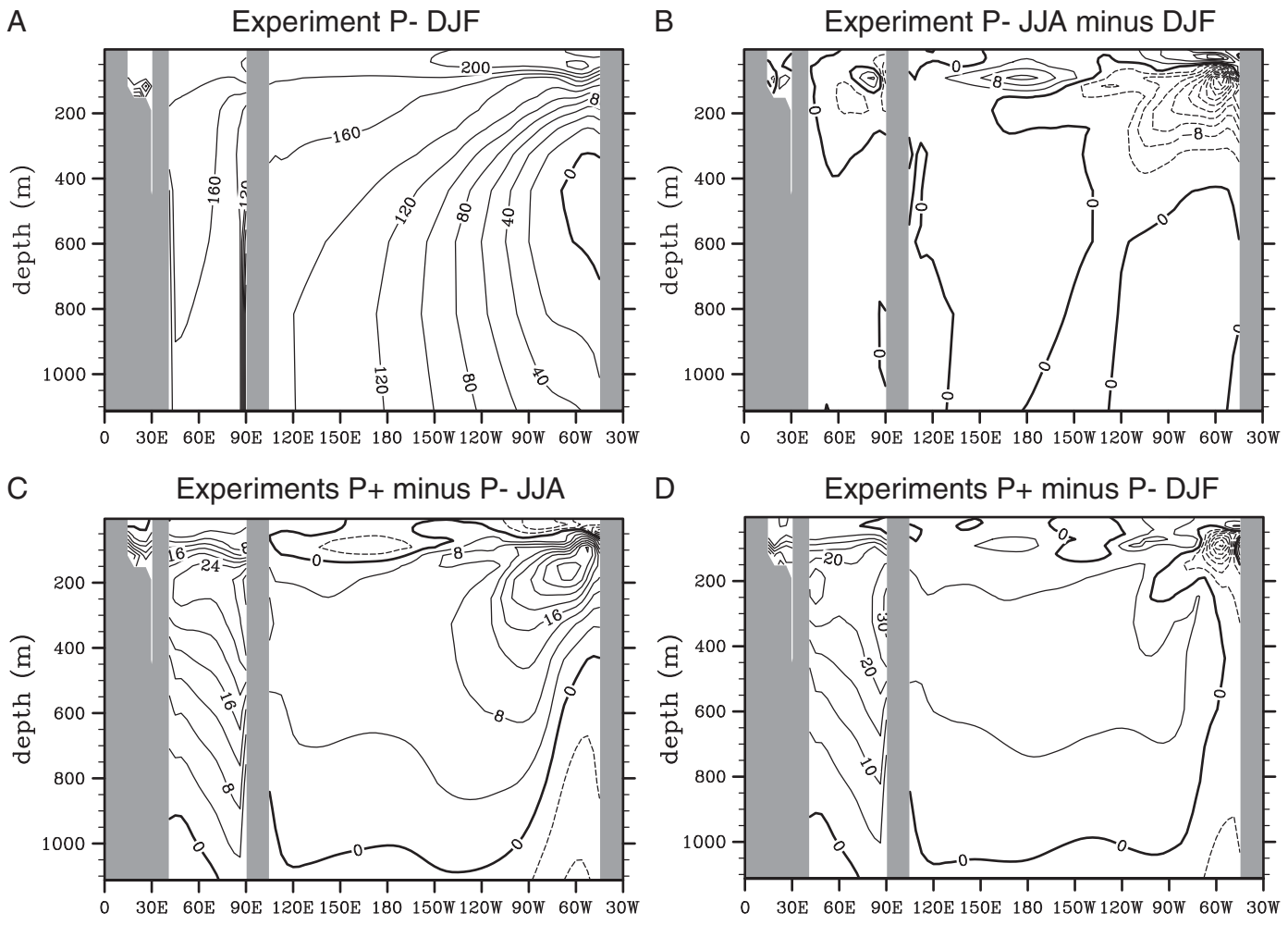

Fig. 10. Upper vertical section of dissolved oxygen (in μmol L^{-1}) through the Tethys Ocean (40°–90°E) and Panthalassa (110°E–40°W) near the equator. (A) DJF for case P–, (B) seasonal variation (JJA minus DJF) for case P−, (C) difference between case P+ and P− for JJA, and (D) difference between case P+ and P− for DJF. The oxygen minimum zone in the eastern equatorial Panthalassa is located between 400 m and 800 m. The gray bar near 90°E is South China. Contour intervals are shown in 20 μmol L^{-1} in (A) and 4 μmol L^{-1} in (B–D).

in the deep Panthalassa. Sulfate pulses into the water masses, stimulating hydrogen sulfide production, may have originated from bioturbation that aerates shallow sediments (Shen et al., 2010), methane release from gas hydrates (Newton et al., 2004), or from volcanic eruptions (Sephton et al., 2005). Euxinia in shallow areas may have been caused either by upward chemocline excursions (Kump et al., 2005; Riccardi et al., 2007; Meyer et al., 2008) or by upwelling of deep or intermediate anoxic water masses (Algeo et al., 2007, 2008) or a combination of both. The simulated orbitally-driven changes in deep-sea circulation and oxygen-distribution in this study are small, suggesting that the deep sea is an unlikely source for periodic upwelling of anoxic water masses. The oxygen minimum zone in intermediate depth, however, might have expanded intermittently due to orbitally driven pulses of enhanced nutrient supply. Orbitally-induced variability of oxygen concentrations appear to be largest in the Tethys Ocean where they might have amplified a decrease in the oxygen concentration due to enhanced nutrient supply to the ocean, due to topographic changes (Osen et al., 2012) or due to a combination of both. The model simulations in this study also confirm findings from previous studies (Winguth and Maier-Reimer, 2005; Meyer et al., 2008; Winguth and Winguth, 2012) that with nutrient inventories across the PTB similar to today, the Panthalassa would not have been euxinic.

There are several limitations associated with this study. For example, topography boundary conditions are not well known for the end-Permian. The presence of mid-ocean ridges can enhance vertical mixing, thereby changing oxygen gradients (see Osen et al., 2012). The position of seaways, like those north and south of Pangea, can change the regional heat fluxes and lead to warming of the adjacent land masses (Winguth et al., 2002). Also, the positions of islands and topographic features in the Tethys Ocean remain uncertain (Scotese and Langford, 1995). A rise of the sill between the Tethys Ocean and the Panthalassa could have contributed to more stagnant water masses and anoxia in the Tethys and could potentially have enhanced sulfidic upwelling (Osen et al., 2012). The height of the Pangean mountain ranges, which is uncertain, could have impacted the intensity of the monsoonal circulation significantly, as discussed for example in Parrish (1993) or in Kutzbach and Gallimore (1989). An increase in the altitude of mountains (Fluteau et al., 2001) or highland plateaus would have led to enhanced sensible and latent heat flux from the surface to overlying air masses, because the surrounding air at high altitude is much cooler due to the lapse rate. This would have caused an intensification of the low-pressure system over land and thus enhanced monsoonal precipitation (Kutzbach et al., 1993), weathering (An et al., 2001) and hence nutrient supply to the Tethys Ocean.

Other uncertainities in boundary conditions are associated with the concentration of greenhouse gasses at the PTB. Recent estimates from Breecker et al. (2010), based on carbon isotope analysis of paleosols, suggest significantly lower atmospheric CO_2 concentrations than inferred for example by Kidder and Worsley (2004). $\delta^{44/40}Ca$ excursions and negative $\delta^{13}C$ excursions in carbonates and organic matter (Baud et al., 1989; Payne et al., 2004) support ocean acidification

Please cite this article as: Winguth, A., Winguth, C., Precession-driven monsoon variability at the Permian–Triassic Implications for anoxia and the mass extinction, Glob. Planet. Change (2012), doi:10.1016/j.gloplacha.2012.06.006

and hence also high atmospheric CO_2 levels (Sobolev et al., 2011), linked to isotopically light carbon emission from the Siberian Traps at the end of the Permian (Payne et al., 2010). An additional uncertainty arises from the possibility of the dependence of precession-modulated climate sensitivity on the atmospheric CO_2 concentration. The amounts of other greenhouse gasses like methane also remain under discussion; large concentrations of methane could have been released by magma intruding Siberian coal basins, triggering strong climatic feedbacks (Retallack, 1999; Heydari and Hassanzadeh, 2003; Svensen et al., 2009; Retallack et al., 2011). Orbital pacing of methane hydrate release could have contributed to a reorganization of carbon pools within the earth system (Lunt et al., 2011).

Another source of uncertainty is the abundance of cloud condensation nuclei (CCN), which affects droplet formation and the albedo level of clouds (Kump and Pollard, 2008). A consideration of changes in the cloud optical depth would likely enhance ocean stratification and possibly lead to stagnation of the deep-sea circulation, as shown by preliminary simulations at NCAR (Jeff Kiehl and Christine Shields, pers. communication).

Finally, dramatic changes in geochemical cycles (Knoll et al., 1996; Beauchamp and Baud, 2002; Berner, 2002; Payne et al., 2004; Kump et al., 2005; Algeo et al., 2010; Wignall et al., 2010) are not considered in this study, for example uncertainties in nutrient inventories driven by variability in climate, weathering, and volcanic emissions. Model studies of Meyer et al. (2008) and Winguth and Winguth (2012) suggest significant impacts on anoxia by eutrophication.

7. Conclusions

The end-Permian is characterized by an extreme climate with mega-monsoons and pronounced continentality. Simulations with a comprehensive climate system model demonstrate the influence of orbitally-driven changes in regional incoming solar radiation on temperature, precipitation and associated runoff. Such climate modulations are supported by lake sediments and variations in red bed formations.

Areas which experienced significant orbital variability are identified by the model results. This knowledge could be useful for collecting data for orbital tuning in the future. Equatorial upwelling and productivity are especially affected by climate variations due to precessional extremes. However, changes in the oxygen concentration in response to seasonal or orbital variability are confined to the uppermost ocean and the OMZ, but do not significantly affect the deep sea. This study also suggests that nutrient inventory changes by climate-induced enhanced weathering could have played a significant role in anoxia variability across the PTB as identified from geochemical analyses of stratigraphic sections from the Tethys Ocean and from the Panthalassa.

Acknowledgments

We thank Christine Shield and Jeff Kiehl at NCAR for providing the initial and boundary conditions for these simulations and for graphical support, and Paul Wignall, Alan M. Haywood, and David Kidder for constructive remarks that improved the quality of the paper. We are also grateful to Chris Scotese and Angela Osen for the improved paleo-bathymetry. All model simulations were done on NCAR computers, supported by NSF. The work is supported by NSF grant EAR-0745817.

References

Algeo, T.J., Twitchett, R.J., 2010. Anomalous Early Triassic sediment fluxes due to elevated weathering rates and their biological consequences. Geology 38, 1023–1026.
Algeo, T.J., Ellwood, B., Nguyen, T.K.T., Rowe, H., Maynard, J.B., 2007. The Permian–Triassic boundary at Nhi Tao, Vietnam: evidence for recurrent influx of sulfidic watermasses to a shallow-marine carbonate platform. Palaeogeography, Palaeoclimatology, Palaeoecology 252, 304–327.
Algeo, T.J., Shen, Y., Zhang, T., Lyons, T.W., Bates, S.M., Rowe, H., Nguyen, T.K.T., 2008. Association of ^{34}S-depleted pyrite layers with negative carbonate $\delta^{13}C$ excursions at the Permian/Triassic boundary: evidence for upwelling of sulfidic deep-ocean watermasses. Geochemistry, Geophysics, Geosystems 9, Q04025, http://dx.doi.org/10.1029/2007GC001823.
Algeo, T.J., Hinnov, L., Moser, J., Maynard, J.B., Elswick, E., Kuwahara, K., Sano, H., 2010. Changes in productivity and redox conditions in the Panthalassic Ocean during the latest Permian. Geology 38, 187–190, http://dx.doi.org/10.1130/G30483.1.
Alroy, J., Marshall, C.R., Bambach, R.K., Bezuskoe, K., Foote, M., Fuersich, F.T., Hansen, T.A., Holland, S.M., Ivany, L.C., Jablonski, D., Jacobs, D.K., Jones, D.C., Kosnik, M.A., Lidgard, S., Low, S., Miller, A.I., Novack-Gottshall, P.M., Olszewskin, T.D., Patzkowsky, M.E., Raup, D.M., Roy, K., Sepkoski Jr., J.J., Sommers, M.G., Wagner, P.J., Webber, A., 2008. Effects of sampling standardization on estimates of Phanerozoic marine diversification. Proceedings of the National Academy of Sciences of the United States of America 98, 6261–6266.
An, Z., Kutzbach, J.E., Prell, W., Porter, S., 2001. Evolution of Asian monsoons and phased uplift of the Himalaya-Tibetan plateau since Late Miocene times. Nature 411, 62–66.
Anderson, R.Y., 2010. Earth as diode: monsoon source of the orbital 100 ka climate cycle. Climate of the Past Discussions 6, 1421–1452.
Bailey, R.J., 2001. Sequence stratigraphy and orbital forcing in Permian (Rotliegend) desert deposits: a discussion. Journal of the Geological Society 158, 785–791.
Barron, E.J., Fawcett, P.J., 1995. The climate of Pangea: a review of climate model simulations of the Permian. In: Scholle, P.A., Peryt, T.M., Ulmer-Scholle, D.S. (Eds.), The Permian of Northern Pangea. : Paleogeography, Paleoclimates, Stratigraphy, 1. Springer-Verlag, New York, pp. 37–52.
Baud, A., Magaritz, M., Holser, W.T., 1989. Permian–Triassic of the Tethys: carbon isotope studies. Geologische Rundschau 78, 649–677.
Beauchamp, B., Baud, A., 2002. Growth and demise of Permian biogenic chert along northwest Pangea: evidence for end-Permian collapse of thermohaline circulation. Palaeogeography, Palaeoclimatology, Palaeoecology 184, 37–63.
Berger, W.H., 1978. Impact of deep sea drilling on paleoceanography. In: Talwani, M., et al. (Ed.), Deep Drilling Results in the Atlantic Ocean: Continental Margins and Paleoenvironment. Am Geophys Union, Washington, D.C., pp. 297–314.
Berner, R.A., 2002. Examination of hypotheses for the Permo–Triassic boundary extinction by carbon cycle modeling. PNAS 99, 4172–4177.
Breecker, D.O., Sharp, Z.D., McFadden, L.D., 2010. Atmospheric CO_2 concentrations during ancient greenhouse climates were similar to those predicted for A.D. 2100. PNAS 107, 576–580.
Broecker, W.S., Peacock, S., 1999. An ecologic explanation for the Permo–Triassic carbon and sulfur isotope shifts. Global Biogeochemical Cycles 13, 1167–1172.
Campbell, I.H., Czamanske, G.K., Fedorenko, V.A., Hill, R.I., Stepanov, V., 1992. Synchronism of the Siberian Traps and the Permian–Triassic boundary. Science 258, 1760–1763, http://dx.doi.org/10.1126/science.258.5089.1760.
Cerling, T.E., 1991. Carbon dioxide in the atmosphere: evidence from Cenozoic and Mesozoic paleosols. American Journal of Science 291, 377–400.
Collins, W.D., Bitz, C.M., Blackmon, M.L., Bonan, G.B., Bretherton, C.S., Carton, J.A., Chang, P., Doney, S.C., Hack, J.J., Henderson, T.B., Kiehl, J.T., Large, W.G., McKenna, D.S., Santer, B.D., Smith, R.D., 2006a. The Community Climate System Model Version 3 (CCSM3). Journal of Climate 19, 2122–2143.
Collins, W.D., Rasch, P.J., Boville, B.A., Hack, J.J., McCaa, J.R., Williamson, D.L., Briegleb, B.P., Bitz, C.M., Lin, S.-J., Zhang, M., 2006b. The formulation and atmospheric simulation of the Community Atmosphere Model Version 3 (CAM3). Journal of Climate 19, 2144–2161.
Crowley, T.J., North, G.R., 1991. Paleoclimatology. Oxford Univ. Press. (339 pp).
Crowley, T.J., Kim, K.-Y., Mengel, J.G., Short, D.A., 1992. Modeling 100,000-year climate fluctuations in pre-Pleistocene timeseries. Science 255, 705–707.
Daugherty, L.H., 1941. The Upper Triassic Flora of Arizona, 526. Carnegie Inst. Washington Pub. 42 pp.
Doney, S.C., Lindsay, K., Fung, I., John, J., 2006. Natural variability in a stable, 1000-yr global coupled climate–carbon cycle simulation. Journal of Climate 19, 3033–3054.
Erwin, D.H., 1994. The Permo–Triassic extinction. Nature 367, 231–236.
Fluteau, F., Besse, J., Broutin, J., Ramstein, G., 2001. The late Permian climate. What can be inferred from climate modelling concerning Pangea scenarios and Hercynian altitude? Palaeogeography, Palaeoclimatology, Palaeoecology 167, 39–71.
Garcia, H.E., Locarnini, R.A., Boyer, T.P., Antonov, J.I., Baranova, O.K., Zweng, M.M., Johnson, D.R., 2010. World Ocean Atlas 2009, volume 3: dissolved oxygen, apparent oxygen utilization, and oxygen saturation. In: Levitus, S. (Ed.), NOAA Atlas NESDIS, 70. U.S. Government Printing Office, Washington, D.C. (344 pp.).
Gent, P.R., Bryan, F.O., Danabasoglu, G., Lindsay, K., Tsumune, D., Hecht, M.W., Doney, S.C., 2006. Ocean chlorofluorocarbon and heat uptake during the twentieth century in the CCSM3. Journal of Climate 19, 2366–2381.
Gibbs, M.T., Rees, P.M., Kutzbach, J.E., Ziegler, A.M., Behling, P.J., Rowley, D.B., 2002. Simulations of Permian climate and comparisons with climate-sensitive sediments. Journal of Geology 110, 33–55.
Hallam, A., Wignall, P.B., 1997. Mass extinctions and their aftermath. Oxford Univ. Press, New York. (330 pp).
Heydari, E., Hassanzadeh, J., 2003. Deev Jahi model of the Permian–Triassic boundary mass extinction: a case for gas hydrates as the main cause of biological crisis on Earth. Sedimentary Geology 163, 147–163.
Hotinski, R.M., Bice, K.L., Kump, L.R., Najjar, R.G., Arthur, M.A., 2001. Ocean stagnation and End-Permian anoxia. Geology 29, 7–10.
Huang, C., Tong, J., Hinnov, L., Chen, Z.Q., 2011. Did the great dying of life take 700 k.y.? Evidence from global astronomical correlation of the Permian–Triassic boundary interval. Geology 39, 779–782, http://dx.doi.org/10.1130/G32126.1.

Please cite this article as: Winguth, A., Winguth, C., Precession-driven monsoon variability at the Permian–Triassic Implications for anoxia and the mass extinction, Glob. Planet. Change (2012), doi:10.1016/j.gloplacha.2012.06.006

Huybers, P., Aharonson, O., 2010. Orbital tuning, eccentricity, and the frequency modulation of climatic precession. Paleoceanography 25, PA4228, http://dx.doi.org/10.1029/2010PA001952.
Isozaki, Y., 1997. Permo-Triassic boundary superanoxia and stratified superocean: records from lost deep sea. Science 276, 235–238.
Kidder, D.L., Worsley, T.R., 2004. Causes and consequences of extreme Permo-Triassic warming to globally equable climate and relation to the Permo-Triassic extinction and recovery. Palaeogeography, Palaeoclimatology, Palaeoecology 203, 207–237.
Kidder, D.L., Worsley, T.R., 2010. Phanerozoic Large Igneous Provinces (LIPs), HEATT (Haline Euxinic Acidic Thermal Transgression) episodes, and mass extinctions. Palaeogeography, Palaeoclimatology, Palaeoecology 295, 162–191.
Kiehl, J., Shields, C.A., 2005. Climate simulation of the latest Permian: implications for mass extinction. Geology 33, 757–760.
Knoll, A.H., Bambach, R.K., Canfield, D.E., Grotzinger, J.P., 1996. Comparative earth history and Late Permian mass extinction. Science 273, 452–457.
Knoll, A.H., Bambach, R.K., Payne, J.L., Pruss, S., Fischer, W.W., 2007. Paleophysiology and end-Permian mass extinction. Earth and Planetary Science Letters 256, 295–313.
Kump, L.R., Pollard, D., 2008. Amplification of Cretaceous warmth by biological cloud feedbacks. Science 320, 195.
Kump, L.R., Pavlov, A., Arthur, M.A., 2005. Massive release of hydrogen sulphide to the surface ocean and atmosphere during intervals of oceanic anoxia. Geology 33, 397–400.
Kutzbach, J.E., Gallimore, R.G., 1989. Pangaean climates: megamonsoons of the megacontinent. Journal of Geophysical Research 94, 3341–3358.
Kutzbach, J.E., Prell, W.L., Ruddiman, W.F., 1993. Sensitivity of Eurasian climate to uplift of the Tibetan Plateau. Journal of Geology 101, 177–190.
Laskar, J., Robutel, P., Joutel, F., Gastineau, M., Correia, A., Levrard, B., 2004. A long term numerical solution for the insolation quantities of the Earth. Astronomy and Astrophysics 428, 261–285.
Lunt, D.J., Ridgwell, A., Sluijs, A., Zachos, J., Hunter, S., Haywood, A., 2011. A model for orbital pacing of methane hydrate destabilization during the Palaeogene. Nature Geoscience 4, 775–778, http://dx.doi.org/10.1038/NGEO1266.
Maier-Reimer, E., 1993. Geochemical cycles in an ocean general circulation model: preindustrial tracer distributions. Global Biogeochemical Cycles 7, 645–677.
Meyer, K.M., Kump, L.R., Ridgwell, A., 2008. Biogeochemical controls on photic-zone euxinia during the end-Permian mass extinction. Geology 36, 747–750.
Najjar, R.G., Orr, J.C., unpublished manuscript. Ocean Carbon-cycle Model Intercomparison Project OCMIP-2 Biotic HOWTO. , http://www.ipsl.jussieu.fr/OCMIP/.
Najjar, R.G., Sarmiento, J.L., Toggweiler, J.R., 1992. Downward transport and fate of organic matter in the ocean: simulations with a general circulation model. Global Biogeochemical Cycles 6, 45–76.
Newton, R.J., Pevitt, E.L., Wignall, P.B., Bottrell, S.H., 2004. Large shifts in the isotopic composition of seawater sulphate across the Permo–Triassic boundary in northern Italy. Earth and Planetary Science Letters 218, 331–345.
Olsen, P.E., Kent, D.V., 1996. Milankovitch climate forcing in the tropics of Pangaea during the Late Triassic. Palaeogeography, Palaeoclimatology, Palaeoecology 122, 1–26.
Oort, A.H., Peixoto, J.P., 1983. Global angular momentum and energy balance requirements from observations. Advances in Geophysics 25, 355–490.
Osen, A., Winguth, A., Winguth, C., Scotese, C., 2012. Sensitivity of Late Permian climate to topographic changes and implications for the mass extinction. Global and Planetary Change, http://dx.doi.org/10.1016/j.gloplacha.2012.01.011.
Parrish, J.T., 1993. Climate of the supercontinent Pangea. Journal of Geology 101, 215–233.
Payne, J.L., Lehrmann, D.J., Wei, J., Orchard, M.J., Schrag, D.P., Knoll, A.H., 2004. Large perturbations of the carbon cycle during recovery from the End-Permian extinction. Science 305, 506–509, http://dx.doi.org/10.1126/science.1097023.
Payne, J.L., Turchyn, A.V., Paytan, A., DePaolo, D.J., Lehrmann, D.J., Yu, M., Wei, J., 2010. Calcium isotope constraints on the end-Permian mass extinction. PNAS 107, 8543–8548.
Raup, D.M., Sepkoski Jr., J.J., 1982. Mass extinction in the marine fossil record. Science 215, 1501–1503.
Rees, P.M., Gibbs, M.T., Ziegler, A.M., Kutzbach, J.E., Behling, P.J., 1999. Permian climates: evaluating model predictions using global paleobotanical data. Geology 27, 891–894.
Retallack, G.J., 1999. Postapocalyptic greenhouse paleoclimate revealed by earliest Triassic paleosols in the Sydney Basin, Australia. Geological Society of America Bulletin 111, 52–70.
Retallack, G.J., Sheldon, N.D., Carr, P.F., Fanning, M., Thompson, C.A., Williams, M.L., Jones, B.G., Hutton, A., 2011. Multiple Early Triassic greenhouse crises impeded recovery from Late Permian mass extinction. Palaeogeography, Palaeoclimatology, Palaeoecology 308, 233–251.
Riccardi, A., Kump, L.R., Arthur, M.A., D'Hondt, S., 2007. Carbon isotopic evidence for chemocline upward excursions during the end-Permian event. Palaeogeography, Palaeoclimatology, Palaeoecology 248, 73–81.
Robinson, P.L., 1973. Palaeoclimatology and continental drift. In: Tarling, D.H., Runcorn, S.K. (Eds.), Implications of Continental Drift to the Earth Sciences, I. Academic Press, London, pp. 449–476.
Scotese, C.R., Langford, R.P., 1995. Pangea and the Palegeography of the Permian. In: Scholle, P.A., Peryt, T.M., Ulmer-Scholle, D.S. (Eds.), The Permian of Northern Pangea. : Paleogeography, Paleoclimates, and Stratigraphy, 1. Springer-Verlag, Berlin, pp. 3–19.
Sephton, M.A., Looy, C., Brinkhuis, H., Wignall, P.B., de Leeuw, J.W., Visscher, H., 2005. Catastrophic soil erosion during the end-Permian biotic crisis. Geology 33, 941–944.
Sepkoski Jr., J., 1995. Patterns of Phanerozoic extinction: a perspective from global data bases. In: Walliser, O.H. (Ed.), Global Events and Event Stratigraphy in the Phanerozoic. Springer-Verlag, New-York, pp. 36–51.
Shen, Y., Farquhar, J., Zhang, H., Masterson, A., Zhang, T., Wing, B.A., 2010. Multiple S-isotopic evidence for episodic shoaling of anoxic water during Late Permian mass extinction. Nature Communications, http://dx.doi.org/10.1038/ncomms1217.
Sloan, L.C., Huber, M., 2001. Eocene oceanic responses to orbital forcing on precessional time scales. Paleoceanography 16, 101–111.
Sobolev, S.V., Sobolev, A.V., Kuzmin, D.V., Krivolutskaya, N.A., Petrunin, A.G., Arndt, N.T., Radko, V.A., Vasiliev, Y.R., 2011. Linking mantle plumes, large igneous provinces and environmental catastrophes. Nature 477, 312–316.
Stein, C.A., Stein, S., 1992. A model for the global variation in oceanic depth and heat flow with lithospheric age. Nature 359, 123–129.
Strauss, H., 1997. The isotopic composition of sedimentary sulfur through time. Palaeogeography, Palaeoclimatology, Palaeoecology 132, 97–118.
Svensen, H., Planke, S., Polozov, A.G., Schmidbauer, Corfu, N.F., Podladchikov, Y.Y., Jamtveit, B., 2009. Siberian gas venting and the end-Permian environmental crisis. Earth and Planetary Science Letters 277, 490–500.
Wanninkhof, R., 1992. Relationship between wind speed and gas exchange over the ocean. Journal of Geophysical Research 97, 7373–7382.
Ward, P.D., Garrison, G.H., Haggart, J.W., Kring, D.A., Beattie, M.J., 2001. Isotopic evidence bearing on Late Triassic extinction events, Queen Charlotte Islands, British Columbia, and implications for the duration and cause of the Triassic/Jurassic mass extinction. Earth and Planetary Science Letters 224, 589–600.
Wignall, P.B., Hallam, A., 1992. Anoxia as a cause of the Permian/Triassic extinction: facies evidence from northern Italy and the western United States. Palaeogeography, Palaeoclimatology, Palaeoecology 93, 21–46.
Wignall, P.B., Hallam, A., 1993. Griesbachian (Earliest Triassic) palaeoenvironmental changes in the Salt Range, Pakistan and south-east China and their bearing on the Permo–Triassic mass extinction. Palaeogeography, Palaeoclimatology, Palaeoecology 102, 215–237.
Wignall, P.B., Newton, R., 2003. Contrasting deep-water records from the Upper Permian and Lower Triassic of South Tibet and British Columbia: evidence for a diachronous mass extinction. Palaios 18, 153–167, http://dx.doi.org/10.1669/0883-1351(2003) 18<153:CDRFTU>2.0.CO;2.
Wignall, P.B., Twitchett, R.J., 1996. Oceanic anoxia and the end Permian mass extinction. Science 272, 1155–1158.
Wignall, P.B., Twitchett, R.J., 2002. Extent, duration, and nature of the Permian–Triassic superanoxic event. In: Koerbl, C., MacLeod, K.G. (Eds.), Catastrophic events and mass-extinctions: Impacts and beyond.Geological Society of America Special Paper 356, 395–413.
Wignall, P.B., Bond, D.P.G., Kuwahara, K., Kakuwa, Y., Newton, R.J., Poulton, S.W., 2010. An 80 million year oceanic redox history from Permian to Jurassic pelagic sediments of the Mino-Tamba terrane, SW Japan, and the origin of four mass extinctions. Global and Planetary Change 71, 109–123.
Winguth, A.M.E., Maier-Reimer, E., 2005. Changes of marine productivity associated with the Permian–Triassic boundary mass extinction: a re-evaluation with ocean general circulation models. Marine Geology 217, 283–304.
Winguth, C., Winguth, A., 2012. Simulating Permian–Triassic oceanic anoxia distribution: implications for species extinction and recovery. Geology 40, 127–130, http://dx.doi.org/10.1130/G32453.1.
Winguth, A.M.E., Heinze, C., Kutzbach, J.E., Maier-Reimer, E., Mikolajewicz, U., Rowley, D.B., Rees, P.M., Ziegler, A.M., 2002. Simulated warm polar currents during the Middle Permian. Paleoceanography 17, 1057, http://dx.doi.org/10.1029/2001PA000646.
Yeager, S.G., Shields, C.A., Large, W.G., Hack, J.J., 2006. The low-resolution CCSM3. Journal of Climate 19, 2545–2566.
Zhang, R., Follows, M.J., Grotzinger, J.P., Marshall, J., 2001. Could the Late Permian deep ocean have been anoxic? Paleoceanography 16, 317–329.
Zhou, Y., Ren, Y., 1981. Gallium distribution in coal of Late Permian coal fields, southwestern China, and its geochemical characteristics in the oxidized zone of coal seams. International Journal of Coal Geology 1, 235–260.
Ziegler, A.M., Hulver, M.L., Rowley, D.B., 1997. Permian world topography and climate. In: Martini, I.P. (Ed.), Late Glacial and Postglacial Environmental Changes: Quaternary, Carboniferous-Permian, and Proterozoic. Oxford University Press, New York, pp. 111–146.
Ziegler, A.M., Gibbs, M.T., Hulver, M.L., 1998. A mini-atlas of oceanic water masses in the Permian period. Proceedings of the Royal Society of Victoria 110, 323–343.
Ziegler, A.M., Eshel, G., McAllister Rees, P., Rothfus, T.A., Rowley, D.B., Sunderlin, D., 2003. Tracing the tropics across land and sea: Permian to present. Lethaia 36, 227–254.

Please cite this article as: Winguth, A., Winguth, C., Precession-driven monsoon variability at the Permian–Triassic Implications for anoxia and the mass extinction, Glob. Planet. Change (2012), doi:10.1016/j.gloplacha.2012.06.006